AIP Applied Physics Letters

Stress mapping of micromachined polycrystalline silicon devices via confocal Raman microscopy

Grant A. Myers, Siddharth S. Hazra, Maarten P. de Boer, Chris A. Michaels, Stephan J. Stranick, Ryan P. Koseski, Robert F. Cook, and Frank W. DelRio

Citation: Applied Physics Letters **104**, 191908 (2014); doi: 10.1063/1.4878616
View online: http://dx.doi.org/10.1063/1.4878616
View Table of Contents: http://scitation.aip.org/content/aip/journal/apl/104/19?ver=pdfcov
Published by the AIP Publishing

Articles you may be interested in
Micro-Raman spectroscopy and analysis of near-surface stresses in silicon around through-silicon vias for three-dimensional interconnects
J. Appl. Phys. **111**, 063513 (2012); 10.1063/1.3696980

High-spatial-resolution Raman microscopy of stress in shallow-trench-isolated Si structures
Appl. Phys. Lett. **89**, 233505 (2006); 10.1063/1.2400057

Raman stress maps from finite-element models of silicon structures
J. Appl. Phys. **100**, 033516 (2006); 10.1063/1.2219899

Silicon micromachining for millimeter-wave applications
J. Vac. Sci. Technol. A **18**, 743 (2000); 10.1116/1.582170

Addendum: "Stress measurements in silicon devices through Raman spectroscopy: Bridging the gap between theory and experiment" [J. Appl. Phys. 79, 7148 (1996)]
J. Appl. Phys. **85**, 7484 (1999); 10.1063/1.369385

AIP Journal of Applied Physics

Journal of Applied Physics is pleased to announce André Anders as its new Editor-in-Chief

This article is copyrighted as indicated in the article. Reuse of AIP content is subject to the terms at: http://scitation.aip.org/termsconditions. Downloaded to IP: 129.6.180.62 On: Wed, 09 Jul 2014 16:15:10

CrossMark click for updates

Stress mapping of micromachined polycrystalline silicon devices via confocal Raman microscopy

Grant A. Myers,[1] Siddharth S. Hazra,[2,a)] Maarten P. de Boer,[2] Chris A. Michaels,[1] Stephan J. Stranick,[1] Ryan P. Koseski,[1,b)] Robert F. Cook,[1] and Frank W. DelRio[1,c)]
[1]*Material Measurement Laboratory, National Institute of Standards and Technology, Gaithersburg, Maryland 20899, USA*
[2]*Department of Mechanical Engineering, Carnegie Mellon University, Pittsburgh, Pennsylvania 15213, USA*

(Received 9 April 2014; accepted 7 May 2014; published online 15 May 2014)

Stress mapping of micromachined polycrystalline silicon devices with components in various levels of uniaxial tension was performed. Confocal Raman microscopy was used to form two-dimensional maps of Raman spectral shifts, which exhibited variations on the scale of the component and on the scale of the microstructure. Finite element analysis models enabled direct comparison of the spatial variation in the measured shifts to that of the predicted stresses. The experimental shifts and model stresses were found to be linearly related in the uniaxial segment, with a proportionality constant in good agreement with calculations based on an opto-mechanical polycrystalline averaging analysis. © *2014 AIP Publishing LLC*.
[http://dx.doi.org/10.1063/1.4878616]

Assessing and optimizing the performance and reliability of mechanical devices requires insight into two elements: (i) the applied stresses produced in the components forming the devices, driving failure, and (ii) the strengths of the materials used to create the components, providing an upper bound to failure resistance. For microelectromechanical systems (MEMS), considerable work has focused on the second of these elements, and many test structures have been developed and demonstrated to investigate the strengths and strength distributions of MEMS components. These include the tensile strengths of bars,[1–10] the bending strengths of straight[11] and curved[12] beams, and the flexure strengths of plates.[13,14] Both polycrystalline silicon (polysilicon)[1–7] and single-crystal silicon (SCS),[8–14] materials commonly used in MEMS device fabrication, have been studied. Less attention has focused on the first element, not least because strain (and hence stress) measurement methods at large scales (e.g., strain gauge) or on thin films (e.g., wafer curvature, X-ray diffraction) are not applicable to MEMS components. Optical digital image correlation has been used on SCS MEMS tensile bars (TBs),[8] but necessitates additional sample preparation. Confocal Raman spectroscopy methods have been more broadly used and applied to SCS MEMS components in bending[15–17] and polysilicon components in uniaxial tension[18–20] and biaxial compression,[15,21,22] building on earlier work on SCS substrates adjacent to microelectronic devices.[23–27] In many of these SCS systems, a relatively simple stress field describable by an analytical model was assumed, and the stress inferred from the confocal Raman data was readily compared with predictions from the models;[16,23,24] in most of these cases, shifts in the Raman spectral peaks are related to one or two of the elements of the stress tensor by simple multiplication. In other SCS systems, where the stress field was more complicated,[25,27] finite element analysis (FEA) was used to predict or interpret the Raman spectra using the complete stress tensor.[16,17,20,25–27] The SCS studies illustrate good quantitative agreement between predictions and measurements of Raman spectral shifts, sometimes confirmed by electron diffraction-based strain measurements,[26,28,29] pointing to the potential for confocal Raman-based methods for measuring stresses and strains in advanced SCS devices. The agreement and potential for polysilicon MEMS devices is less clear: Although early studies revealed the ability to measure Raman spectral shifts as a function of location on MEMS components[15,18,21,22] and used an opto-mechanical polycrystalline averaging analysis[30] to calculate the multiplicative relationship between shifts and stress, there was no independent measurement or model of stress for comparison. Later studies utilized a separate experimental determination of the multiplicative relationship to interpret shifts as stress for polysilicon MEMS beams, but used an off-device method[19] to determine the relationship or a SCS relationship[20] to compare Raman-inferred polysilicon stresses with FEA. In this Letter, confocal Raman microscopy (CRM) is utilized to measure stress in polysilicon tensile testing devices in a validated quantifiable manner. Components of the devices are placed in various levels of uniaxial tension and two-dimensional maps of Raman spectral shifts are formed, extending the one-dimensional line scans of previous works. FEA-based models of the devices allow for direct comparison of the *spatial variation* of predicted and measured stresses, and polycrystalline opto-mechanical analysis enables direct comparison of the *magnitude* of predicted and measured stresses.

A schematic diagram of the tensile testing device is shown in Fig. 1(a). The device concept, along with the modeling and optimization that led to the current design, are discussed in great detail in previous work.[6,7] In short, the upper end of the TB is fixed to the substrate via a support structure, while the lower end of the TB is connected to a freestanding crosshead with displacement gauges and the female ends of

[a)]Present address: Ostendo Technologies, Carlsbad, California 92011, USA.
[b)]Present address: Saint-Gobain, Marlborough, Massachusetts 01752, USA.
[c)]Author to whom correspondence should be addressed. Electronic mail: frank.delrio@nist.gov

 © 2014 AIP Publishing LLC

This article is copyrighted as indicated in the article. Reuse of AIP content is subject to the terms at: http://scitation.aip.org/termsconditions. Downloaded to IP: 129.6.180.62 On: Wed, 09 Jul 2014 16:15:10

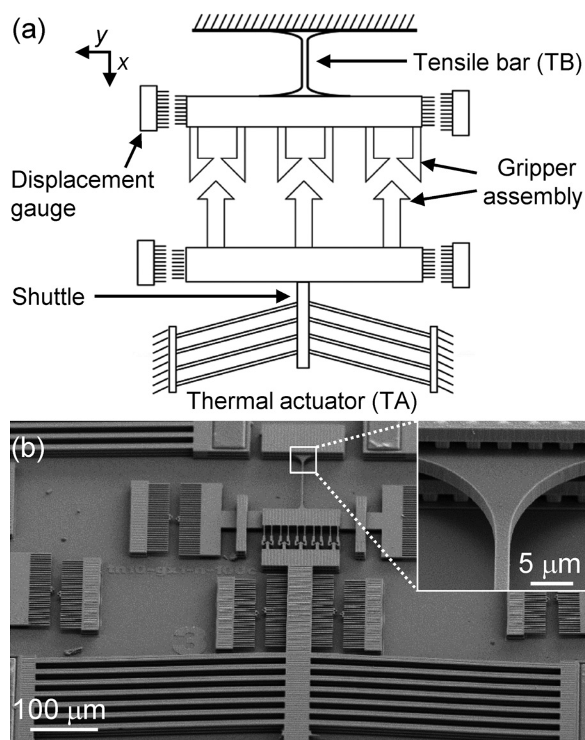

FIG. 1. (a) Schematic diagram and (b) scanning electron microscopy image of a micromachined tensile testing device. Joule-heating-induced expansion of the TA legs results in shuttle motion and gripper insertion, whereas cooling-induced contraction of the legs results in gripper engagement and TB loading. Stress mapping of the TB fillet region in the inset of (b) was performed for various *N*.

a prehensile gripping assembly. The lower part of the device consists of a shuttle that connects the corresponding male ends of the gripping assembly to a chevron-type thermal actuator (TA) with N leg pairs. A voltage V is applied across the TA legs to engage the gripping assembly and load the TB. As V increases, Joule-heating-induced expansion of the legs induces shuttle motion and eventually gripper insertion. As V decreases, cooling-induced contraction of the TA legs results in gripper engagement and TB loading, with the magnitude of the applied force dependent on N. Because the constitutive behavior of a TA is inherently nonlinear, an accurate assessment of the forces F and displacements d created throughout the device is facilitated here with two numerical models. In the first model, a coupled finite difference analysis (FDA)-FEA approach was employed to calculate F and d of the TA during the insertion, engagement, and loading stages; the FDA portion was used to calculate the temperature distribution along the TA legs, which was then transferred to the FEA portion to calculate both the compressive and tensile F exerted by the TA. Further model details are given in a previous report.[31] In the second model, the TB was fixed on the upper end and loaded to the maximum tensile TA force from the prior model on the lower end to assess the stress parallel to the TB (x-direction) σ_x as a function of N. The FEA simulations were performed under plane stress conditions with quadratic elements and an iterative mesh refinement based on a von Mises stress error indicator. Both models assumed linear-elastic isotropic properties for polysilicon: Young's modulus $E = 164\,\text{GPa}$ and Poisson's ratio $\nu = 0.23$.[32]

The devices were fabricated using the Sandia Ultra-planar Multi-level MEMS Technology (SUMMiT V™) process[33] as described earlier.[6,7] The fabrication process consisted of depositing, patterning, and etching four polysilicon layers separated by three sacrificial silicon dioxide layers; the TB was formed in the third polysilicon layer, resulting in a TB width $w = 1.8\,\mu\text{m}$ and thickness $t = 2.25\,\mu\text{m}$. The sacrificial layers were removed with a hydrofluoric acid solution and the parts were rendered freestanding via CO_2 critical point drying. A field-emission scanning electron microscopy (FESEM) image of a completed device is shown in Fig. 1(b), with a magnified image of the TB fillet region shown in the inset. The gripper assembly in each device was engaged by applying $V \approx 6.5\,\text{V}$ to the TA, at which point the voltage was decreased to $V = 0\,\text{V}$ and the TB was loaded, but not broken (only devices with N from 3 to 8 were examined because the resulting TB stresses were less than the fracture stress of the polysilicon). The TB fillet region of each device was then imaged via CRM at Raman shifts ω ranging from $400\,\text{cm}^{-1}$ to $700\,\text{cm}^{-1}$, as described previously.[34] Briefly, fiber-coupled 488-nm laser light was reflected off an inject-reject style long-pass filter and focused on a sample surface using a 100× oil immersion lens (NA = 1.40). The scattered light was collected through the lens and long-pass filter and focused into a multimode fiber coupled to a holographic spectrograph and a liquid N_2-cooled charge-coupled device camera for analysis. The sample was mounted on a closed-loop piezoelectric stage for scanning in ambient conditions; the 10 nm stage resolution allowed for ≈200 nm spatial resolution with oversampling. Individual spectra were measured with ≈1 mW laser power and 1 s integration time for a signal-to-noise ratio >500:1 and then fit to a Pearson-VII lineshape function to assess the Raman spectral peak positions ω_p with respect to the peak position from the substrate spectrum. The resulting peak position maps were taken over a $(20 \times 20)\,\mu\text{m}^2$ region with (128×128) pixels. The maps were masked to remove the data from the substrate region that is of no interest for this study, leaving only the spectral data from the TB fillet region. The criterion for defining the mask regions was based on the spatial derivative of the spectral intensity across a row; the transition from the sample being in focus (TB fillet region) to out-of-focus (substrate) was indicated when the derivative reached a maximum. Temperature-induced changes in the spectral data were curtailed by (1) reducing the voltage across the TA to zero after gripper engagement and TB loading and (2) minimizing the laser power.

Figure 2(a) summarizes the results from the coupled FDA-FEA model during the insertion, engagement, and loading stages of the TA as a function of N. In the insertion stage, Joule-heating-induced expansion of the legs results in shuttle motion, which can induce a compressive force in the TA as given by the solid lines in Fig. 2(a). The compressive F decreased nonlinearly as d increased, until ultimately reaching zero at the maximum d. The devices were designed with maximum d large enough to guarantee full gripper engagement, but small enough to require $V < 6.5\,\text{V}$, thus ensuring temperatures below the recrystallization temperature of polysilicon (≈600 °C). In the loading stage, cooling-induced contraction of the legs results in gripper

This article is copyrighted as indicated in the article. Reuse of AIP content is subject to the terms at: http://scitation.aip.org/termsconditions. Downloaded to IP: 129.6.180.62 On: Wed, 09 Jul 2014 16:15:10

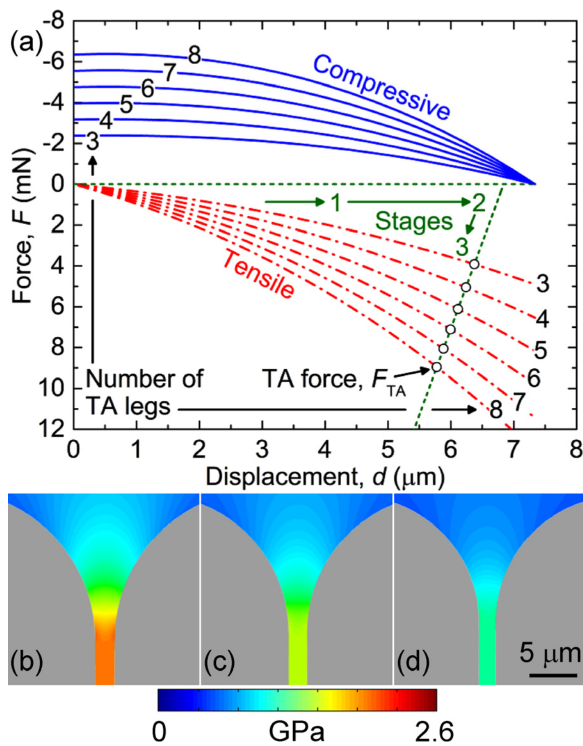

FIG. 2. FEA of the tensile testing device. In (a), the TA forces and displacements during the insertion (1), engagement (2), and loading (3) stages are calculated via a coupled FDA-FEA model. The resulting F_{TA} values are used in a subsequent FEA model of the TB fillet region to create σ_x maps as a function of N; the stress maps for (b) 8, (c) 5, and (d) 3 leg pairs are shown.

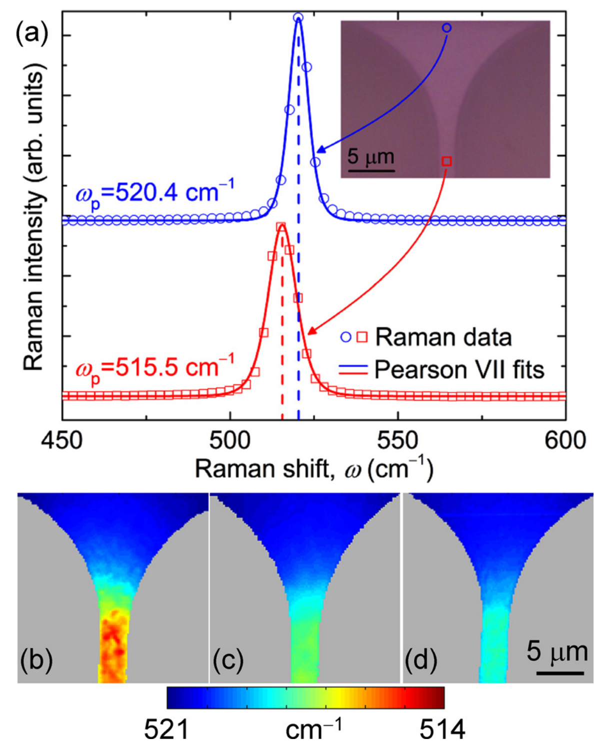

FIG. 3. CRM of the tensile testing device. Raman spectra are obtained at (128 × 128) pixels over the TB fillet region (only two shown in (a) for clarity) and the positions of the peak intensities are found by fitting the data to a Pearson VII function. The resulting ω_p values are used to create ω_p maps for all N; the wavenumber maps for (b) 8, (c) 5, and (d) 3 leg pairs are shown.

engagement, which induces a tensile force in the TB. The maximum possible tensile force F_{TA} for each N occurs when the TA cools to ambient and is equivalent to the equilibrium force between the TA and TB as calculated at the intersection of the load lines for the TA (dotted-dashed lines) and the TB (dashed lines). As illustrated by the circles in Fig. 2(a), F_{TA} increased monotonically from 3.9 mN to 9.0 mN as N increased from 3 to 8; the relationship between F_{TA} and N was found to be slightly nonlinear due to compliance in the device. As previously described, these F_{TA} values were then utilized in the second FEA model to determine σ_x in the TB fillet region as a function of N; the resulting σ_x maps for N of 8, 5, and 3 are shown in Figs. 2(b)–2(d), respectively. In all three maps, σ_x was small near the fixed end of the TB and increased to a maximum value in the gauge section. The maximum values for σ_x increased from 1.0 GPa to 2.2 GPa as N increased from 3 to 8; the σ_x are less than most of the reported fracture σ_x for these devices,[7] indicating that the threshold N for fracture is between 8 and 10. As expected, the TB is in uniaxial stress in the gauge region, with σ_x being the only non-zero stress component. In contrast, the stress state outside of the gauge region is more complicated, as it includes additional normal and shear components.

Figure 3(a) shows CRM measurements from two locations on a TB with $N = 8$, along with Pearson VII fits to determine ω_p. In the top (blue) spectrum, $\omega_p \approx 520\,\text{cm}^{-1}$, which corresponds to the "stress-free" spectral peak position for silicon. In the bottom (red) spectrum, ω_p has shifted to a smaller value by $\approx 5\,\text{cm}^{-1}$, consistent with a tensile stress field. As previously described, such ω_p values were used to generate maps over the TB as a function of N; the resulting ω_p maps for N of 8, 5, and 3 are shown in Figs. 3(b)–3(d), respectively. In all three maps, $\omega_p \approx 520\,\text{cm}^{-1}$ near the fixed end of the TB and decreased towards the gauge section of the TB. The average ω_p in the gauge section decreased from $(518.7 \pm 0.1)\,\text{cm}^{-1}$ to $(516.0 \pm 0.3)\,\text{cm}^{-1}$ as N increased from 3 to 8 (experimental uncertainties are one standard deviation of the population mean), in agreement with the FEA results that suggest an increase in σ_x with N. Unlike the FEA, however, there is variability in ω_p within the gauge section, as shown in Fig. 3(b). One potential explanation for the variability is the polysilicon grain structure. The grains have a mixed equiaxed and columnar morphology and an isotropic distribution of orientations, with sizes ranging from 0.1 μm to 3 μm.[32,35] The variations in ω_p thus occurred over length scales similar to the grain size and are likely due to variations in the grain boundary inclination angles, triple point locations, and crystal orientations and anisotropy.[36]

In Fig. 4(a), the σ_x results from FEA and the ω_p results from CRM are plotted as a function of x along the TB centerline for N of 8, 5, and 3. Overall, there is good agreement between the FEA simulations and CRM experiments. In detail, σ_x and ω_p vary as a function of x outside of the gauge section, but are relatively constant in the gauge section (oscillations are likely due to variability in the grain structure, as suggested earlier). The latter result is due to the uniaxial stress state in the TB. The relationship between σ_x and ω_p for the simple case of uniaxial tension can thus be ascertained by examining the average gauge section σ_x as a

This article is copyrighted as indicated in the article. Reuse of AIP content is subject to the terms at: http://scitation.aip.org/termsconditions. Downloaded to IP: 129.6.180.62 On: Wed, 09 Jul 2014 16:15:10

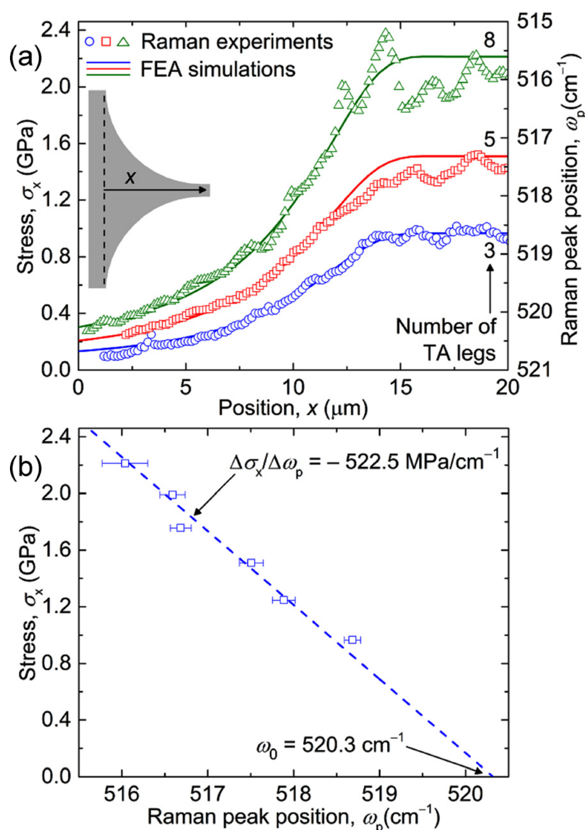

FIG. 4. CRM-FEA comparison for the tensile testing device. In (a), σ_x from FEA and ω_p from CRM are plotted for each pixel along the TB centerline for 8, 5, and 3 leg pairs. In (b), the average gauge section σ_x from FEA are plotted as a function of the average gauge section ω_p from CRM for all N; a line with a $-522.5\,\text{MPa/cm}^{-1}$ slope and a $520.3\,\text{cm}^{-1}$ x-intercept is shown.

function of the average gauge section ω_p, as shown in Fig. 4(b). It is clear from the results that σ_x and ω_p are linearly related. The proportionality constant characterizing the linearity can be calculated from the opto-mechanical polycrystalline averaging analysis of Anastassakis and Liarokopis.[30] In this analysis, the elements of the single-crystal phonon deformation potential (pdp) tensor (linking Raman peak shifts to strain tensor elements) are averaged to generate isotropic polycrystalline pdp values in much the same way as elements of the single-crystal elastic constant tensor (linking the stress and strain tensors) are averaged to calculate isotropic polycrystalline elastic constants.[37,38] These polycrystalline values are then used to calculate the proportionality constant, depending on the stress state. Using the SCS elastic constants of McSkimin and Andreatch[39] and the SCS pdp of Anastassakis *et al.*,[40] the calculated proportionality constant for polysilicon in uniaxial tension is $-522.5\,\text{MPa/cm}^{-1}$. A best-fit line of this slope using the intercept as the fitting parameter is shown in Fig. 4(b); the line fits the measured data very well and results in a zero-stress peak position of $520.3\,\text{cm}^{-1}$, consistent with the stress-free peak positions in Fig. 4(a). Furthermore, if the polysilicon proportionality constant of $-522.5\,\text{MPa/cm}^{-1}$, rather than the [110] SCS proportionality constant of $-434\,\text{MPa/cm}^{-1}$,[15,16,26,27] is used to convert the peak-shift measurements of Beechem *et al.*,[20] agreement with their FEA predictions is obtained. The value of $\approx -420\,\text{MPa/cm}^{-1}$ obtained by Starman *et al.*[19] in their separate polysilicon bending experiments suggests significant compliance between the sample and the strain measurement point or significant influence of less stressed material at the sample neutral plane.

In conclusion, confocal Raman microscopy appears as an extremely useful tool for assessing the stress side of the "stress-strength" considerations used to optimize polysilicon MEMS (and other, e.g., solar cell) device performance and reliability. In the CRM implementation, stress maps can be generated, revealing variations in stress on the scale of the component and on the scale of the microstructure (Fig. 3) and thus enabling identification of strength-controlling defects. Quantitative agreement between CRM measurements, FEA models, and calculations based on independent SCS property values (Fig. 4) implies considerable accuracy and precision for the approach, allowing for a direct, absolute comparison with strength measurements. Future work will look to further explore the variations in the CRM maps on the scale of the microstructure, the sensitivity of the boundary conditions in the FEA models, and the polycrystalline averaging process to predict Raman shifts.

[1] W. N. Sharpe, K. M. Jackson, K. J. Hemker, and Z. Xie, J. Microelectromech. Syst. **10**, 317 (2001).
[2] I. Chasiotis and W. G. Knauss, J. Mech. Phys. Solids **51**, 1533 (2003).
[3] I. Chasiotis and W. G. Knauss, J. Mech. Phys. Solids **51**, 1551 (2003).
[4] B. L. Boyce, J. M. Grazier, T. E. Buchheit, and M. J. Shaw, J. Microelectromech. Syst. **16**, 179 (2007).
[5] B. L. Boyce, Exp. Mech. **50**, 993 (2010).
[6] S. S. Hazra, M. S. Baker, J. L. Beuth, and M. P. de Boer, J. Micromech. Microeng. **19**, 082001 (2009).
[7] S. S. Hazra, M. S. Baker, J. L. Beuth, and M. P. de Boer, J. Microelectromech. Syst. **20**, 1043 (2011).
[8] L. Banks-Sills, J. Shklovsky, S. Krylov, H. A. Bruck, V. Fourman, R. Eliasi, and D. Ashkenazi, Strain **47**, 288 (2011).
[9] M. S. Gaither, F. W. DelRio, R. S. Gates, and R. F. Cook, J. Mater. Res. **26**, 2575 (2011).
[10] M. S. Gaither, R. S. Gates, R. Kirkpatrick, R. F. Cook, and F. W. DelRio, J. Microelectromech. Syst. **22**, 589 (2013).
[11] T. Namazu, Y. Isono, and T. Tanaka, J. Microelectromech. Syst. **9**, 450 (2000).
[12] R. Kirkpatrick, W. A. Osborn, M. S. Gaither, R. S. Gates, F. W. DelRio, and R. F. Cook, MRS Commun. **3**, 113 (2013).
[13] K. S. Chen, A. Ayon, and S. M. Spearing, J. Am. Ceram. Soc. **83**, 1476 (2000).
[14] K. S. Chen, A. Ayon, X. Zhang, and S. M. Spearing, J. Microelectromech. Syst. **11**, 264 (2002).
[15] M. Siakavellas, E. Anastassakis, G. Kaltsas, and A. G. Nassiopoulos, Microelectron. Eng. **41/42**, 469 (1998).
[16] V. T. Srikar, A. K. Swan, M. S. Unlu, B. B. Goldberg, and S. M. Spearing, J. Microelectromech. Syst. **12**, 779 (2003).
[17] F. Urena, S. H. Olsen, and J.-P. Raskin, J. Appl. Phys. **114**, 144507 (2013).
[18] H. Talaat, S. Negm, H. E. Schaffer, F. Adar, and A. G. Nassiopoulos, Appl. Surf. Sci. **123/124**, 742 (1998).
[19] L. A. Starman, J. A. Lott, M. S. Amer, W. D. Cowan, and J. D. Busbee, Sens. Actuat. A **104**, 107 (2003).
[20] T. Beechem, S. Graham, S. P. Kearney, L. M. Phinney, and J. R. Serrano, Rev. Sci. Instrum. **78**, 061301 (2007).
[21] G. Kaltsas, A. G. Nassiopoulos, M. Siakavellas, and E. Anastassakis, Sens. Actuat. A **68**, 429 (1998).
[22] H. Talaat, S. Negm, H. E. Schaffer, G. Kaltsas, and A. G. Nassiopoulos, J. Non-Crystal. Solids **266–269**, 1345 (2000).
[23] I. De Wolf, J. Vanhellemont, A. Romano-Rodriguez, H. Norstrom, and H. E. Maes, J. Appl. Phys. **71**, 898 (1992).
[24] I. De Wolf, H. E. Maes, and S. K. Jones, J. Appl. Phys. **79**, 7148 (1996).
[25] Q. Ma, S. Chiras, D. R. Clarke, and Z. Suo, J. Appl. Phys. **78**, 1614 (1995).
[26] V. Senez, A. Armigliato, I. De Wolf, G. Carnevale, R. Balboni, S. Frabboni, and A. Benedetti, J. Appl. Phys. **94**, 5574 (2003).

This article is copyrighted as indicated in the article. Reuse of AIP content is subject to the terms at: http://scitation.aip.org/termsconditions. Downloaded to IP: 129.6.180.62 On: Wed, 09 Jul 2014 16:15:10

[27]R. P. Koseski, W. A. Osborn, S. J. Stranick, F. W. DelRio, M. D. Vaudin, T. Dao, V. H. Adams, and R. F. Cook, J. Appl. Phys. **110**, 073517 (2011).
[28]M. D. Vaudin, Y. B. Gerbig, S. J. Stranick, and R. F. Cook, Appl. Phys. Lett. **93**, 193116 (2008).
[29]M. D. Vaudin, G. Stan, Y. B. Gerbig, and R. F. Cook, Ultramicroscopy **111**, 1206 (2011).
[30]E. Anastassakis and E. Liarokapis, J. Appl. Phys. **62**, 3346 (1987).
[31]M. S. Baker, R. A. Plass, T. J. Headley, and J. A. Walraven, Technical Report No. SAND2004–6635, Sandia National Laboratories, Albuquerque, NM, 2004.
[32]B. D. Jensen, M. P. de Boer, N. D. Masters, F. Bitsie, and D. A. LaVan, J. Microelectromech. Syst. **10**, 336 (2001).
[33]J. J. Sniegowski and M. P. de Boer, Annu. Rev. Mater. Sci. **30**, 299 (2000).
[34]Y. B. Gerbig, S. J. Stranick, D. J. Morris, M. D. Vaudin, and R. F. Cook, J. Mater. Res. **24**, 1172 (2009).
[35]M. T. Dugger, B. L. Boyce, T. E. Buchheit, and S. V. Prasad, Technical Report No. SAND2004–1319, Sandia National Laboratories, Albuquerque, NM, 2004.
[36]M. Kamaya, Y. Kawamura, and T. Kitamura, Int. J. Solid Struct. **44**, 3267 (2007).
[37]R. Hill, Proc. Phys. Soc. A **65**, 349 (1952).
[38]H. J. Juretschke, *Crystal Physics* (Benjamin, Reading, MA, 1974).
[39]H. J. McSkimin and P. Andreatch, J. Appl. Phys. **35**, 2161 (1964).
[40]E. Anastassakis, A. Cantarero, and M. Cardona, Phys. Rev. B **41**, 7529 (1990).

This article is copyrighted as indicated in the article. Reuse of AIP content is subject to the terms at: http://scitation.aip.org/termsconditions. Downloaded to IP: 129.6.180.62 On: Wed, 09 Jul 2014 16:15:10